2011

Four-window technique for measuring optical-phase-space-time-frequency tomography

Rachel A. Blaser
Michigan Technological University

FOUR-WINDOW TECHNIQUE FOR MEASURING OPTICAL-PHASE-SPACE-TIME-FREQUENCY TOMOGRAPHY

By

Rachel A. Blaser

A REPORT

Submitted in partial fulfillment of the requirements for the degree of

MASTER OF SCIENCE

Physics

MICHIGAN TECHNOLOGICAL UNIVERSITY

2011

This report, "Four-window technique for measuring optical-phase-space-time-frequency tomography," is hereby approved in partial fulfillment of the requirements for the Degree of MASTER OF SCIENCE IN PHYSICS.

Department of Physics

Signatures:

Report Advisor   _____
Dr. Kim Fook Lee

Committee Member   _____
Dr. Miguel Levy

Committee Member   _____
Dr. John Jaszczak

Committee Member   _____
Dr. Durdu Guney

Department Chair _____
Dr. Ravi Pandey

Date _____

Abstract

A new approach, the four-window technique, was developed to measure optical phase-space-time-frequency tomography (OPSTFT). The four-window technique is based on balanced heterodyne detection with two local oscillator (LO) fields. This technique can provide independent control of position, momentum, time and frequency resolution. The OPSTFT is a Wigner distribution function of two independent Fourier transform pairs, phase-space and time-frequency. The OPSTFT can be applied for early disease detection.

Table of Contents

Table of Figures

Chapter 1 Introduction

1.1 Biomedical Application and Motivation

Motivation for developing optical phase-space-time-frequency tomography (OPSTFT) is to non-invasively identify epithelial cancers at an earlier stage. In 2009 more than half a million people died from epithelial cancers and 1,262,510 new epithelial cancer cases were reported in the U.S.[1] Current methods used for identifying tumors include x-ray, CT, PET and MRI [1,2,3,4,5]. For these methods the tumor must be 10mm-100mm before it can be seen.[6] These imaging techniques have to be followed by a biopsy of the tumor to confirm malignancy. The biopsy requires general anesthesia [1,4]. Current methods, require dyes, tissue sectioning, fixation, and exposure to radiation, have higher rates of false positive results.[1,4,5]

Low coherence optical tomography shows promise as a non-invasive tool for detecting early stage epithelial cancers. Optical tomography is based on near infrared light passing through the tissue and then emerging containing valuable information.[7] Optical coherence tomography has high resolution, high penetration depth, high sensitivity and specificity. These attributes allow accurate assessment of tissue function, cell function and morphology *in situ*. This optical method uses near infrared wavelengths, unlike x-ray imaging and MRI.[6] At these wavelengths, it allows for detection of abnormal metabolic processes which lead to tumor formation. The current methods only respond to large structural damage. [6,7] Detection of the cancer at a much earlier stage would significantly improve the chance for patient survival.[1,4,5]

Optical phase-space-time-frequency tomography can also be used for lymphedema detection. Lymphedema is the swelling of arms or legs caused by a block in the lymphatic system. When there is a block, the lymph fluid cannot drain and the fluid buildup causes the limbs to swell. Some cancer treatments include the removal of lymph nodes which is the most common cause of lymphedema.

A collaborator from the biomedical engineering department at Michigan Technological University studies lymphedema in mice. Figure 1a and 1b shows mouse tail skin for normal skin and swollen skin, similar to the same affect in human tissue.
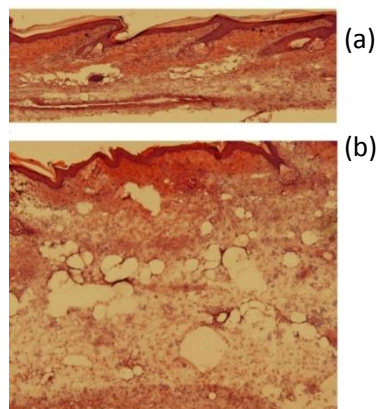

(a)

(b)

Figure 1 (a) shows normal tissue and (b) shows swollen tissue**.**

The normal tissue and the swollen tissue are obtained by cutting the mouse tail as shown in Figure 2a and 2b. Optical phase-space-time-frequency tomography can be used to non-invasively detect and study the differences in the swollen tissues compared to the normal tissues.
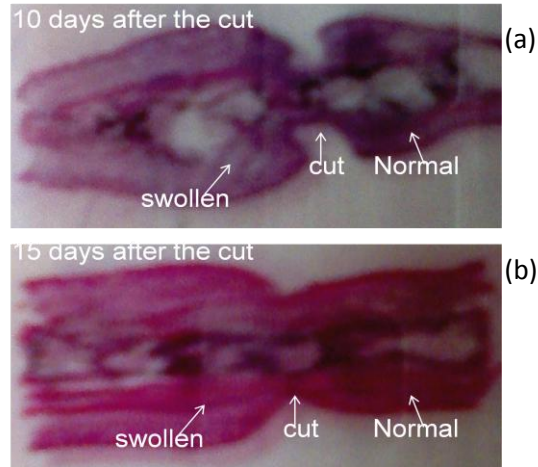
Figure 2 (a) and (b) show the cut rat tail tissue and the difference in swelling over time.

1.2 Related Work

In a study by John W. Pyhtila, et. al. at Durham, North Carolina[8] frequency(ω) - angle(p) resolved low coherence interferometry (fa/LCI) was applied to imaging tissue. The fa/LCI used was a modified Mach-Zehnder interferometer. A superluminescent diode (SLD) with wavelength of 841.5nm was used.[8] The light from the SLD was sent through a fiber bundle and split into reference and input beams by a fiber splitter. The scattered light from the human esophagus tissue sample was collected by a Fourier lens. This Fourier transformed the angle(p) distribution of the scattered field and converted it to a spatial(x) distribution.[8] The distribution provided the nuclear diameter and density as a function of depth beneath the tissue surface. Their results showed a significant increase in the size of dysplastic cell nuclei compared to normal cells. The cells were on a scale of 2-20µm.[8] Human cell size can range from 8-30 µm and the average size for human cell nucleus is 1.7 µm.[11]

In another study, researchers from Duke, MIT, OSU and the National Cancer Institute showed similar results to the above study. Again it was found that dysplastic cells were larger than normal cells.[9,10] This study used angle-resolved low-coherence interferometry (a/LCI). A modified Michelson interferometer was used with a SLD of wavelength 845nm. [9] The light from the SLD was divided into the reference and input beams by a beam splitter. The reference beam was reflected and recombined at the beam splitter with the input beam light reflected off the sample. The mixed fields create an interference pattern. A heterodyne signal was then created by translating the reference mirror at a rate of 4mm/s. The heterodyne signal oscillated at a corresponding Doppler-shift frequency. The beat intensity of the field was determined by calculating

the power spectrum of the digitized photocurrent and then band-passing the signal. This study found the mean sizes of cell nuclei in rat esophagus epithelial tissue for normal, low grad dysplasia, high grade dysplasia and apoptotic cell as follows; 9.7 µm, 11.4 µm, 14.7 µm, 5.8 µm, respectively.[9] These results were compared to photomicrographs of the same tissues to confirm their histological classification.

Current histology imaging and classification shows that dysplastic cell nuclei are larger compared to cell nuclei in healthy tissue. [1,4,5] Developing optical phase-space-time-frequency tomography will allow for more information to better detect diseased tissues.

1.3 Organization
The remainder of this report is as follows:

- Chapter 1 – Introduction
- Chapter 2 – This section explores the conceptual basis of the imaging technique used.
- Chapter 3 – This section shows previous and current theoretical approach.
- Chapter 4 –This section gives details about the simulations conducted and the results of the simulations.
- Chapter 5 – Conclusion

Chapter 2 Background

2.1 Wigner Function
The Wigner function is a quasi-probability density that provides a connection between the wave function in Schrodinger's equation to a probability distribution in phase space. The wave function cannot be measured directly; therefore the wave function can be represented by the Wigner function. The definition of the Wigner function is given in Eq. (1).
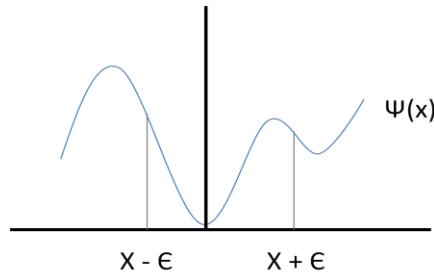

Figure 3 shows the wave function and the integration point as seen in Eq. (1).

$$W(x,p) = \int e^{i\epsilon p} \langle \Psi^*(x+\epsilon)\Psi(x-\epsilon) \rangle \tag{1}$$

A very important property of the Wigner function is that it does not have to be positive definite. The fact that it can have a negative value implies that a particle at a given time cannot have definitive position and momentum coordinates.[12,13,14] This is a unique property in quantum mechanics. The Wigner distribution for a wave field that varies in the spatial and frequency domain, $E(x, \omega)$, is shown by the equation below.[15]

$$W(x,p,\omega,t) = \int \frac{d\varepsilon}{2\pi} e^{i\varepsilon p} \int \frac{d\Omega}{2\pi} e^{i\Omega t} \langle E^* \left(x + \frac{\varepsilon}{2}, \omega + \frac{\Omega}{2} \right) E \left(x - \frac{\varepsilon}{2}, \omega - \frac{\Omega}{2} \right) \rangle \qquad (2)$$

From Eq. (2) it can be easily shown that $\iint W(x,p,\omega,t)dpdt = |E(x,\omega)|^2$, $\iint W(x,p,\omega,t)dxd\omega = |E(p,t)|^2$ and so forth for each of the variable sets. A very essential point about Eq. (2) is that the mutual coherence function and Wigner function are linked by a Fourier Transform in position and frequency (spectra). This shows that the Wigner function is sensitive to changes in spatial and spectra coordinates. Therefore changing these coordinates varies the phase and amplitude of the wave field.[15]

2.2 Phase Space

The goal is to measure the Wigner function in terms of position and momentum coordinates. For a classical field, the position is the X⊥ - vector and the momentum is the K –vector of the wave field as seen in Figure 4. In this case the transverse momentum, K⊥ , of the field is measured. If there is a Gaussian beam along K∥ then the transverse momentum is given by the following relations,

$$P_\perp = k_\perp = \theta K \qquad (3)$$

$$K = \frac{2\pi}{\lambda} \qquad (4)$$

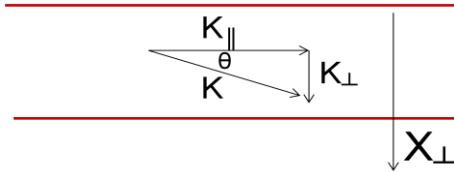where theta is the angle between this k-vector and the optical axis.

Figure 4 shows the transverse position and transverse momentum.

4

2.3 Balanced Heterodyne Detection

A schematic of balanced heterodyne detection is shown in Figure 5. Two apertures can be used in a balanced heterodyne detection scheme to measure the Wigner distribution. A super luminescent diode (SLD) is used as the source beam which is then split into the LO and signal beams. The LO and signal beam are mixed at the 50-50 beam splitter. The photodiode detectors, D1 and D2, receive the two outputs from the beamsplitter. This setup is arranged so that the photocurrents from the photodiodes are subtracted. An advantage of this detection scheme is that a strong local oscillator beam can be used to detect a weak signal beam. This scheme can cancel out the thermal noise. The Wigner phase-space distribution for the signal beam is obtained by changing the position of the local oscillator beam by translating Mirror 1 by a distance d_x and the momentum by moving the Lens 1 by d_p.
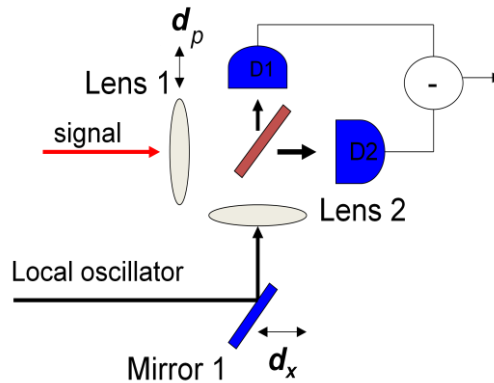
Figure 5 shows the balanced heterodyne detection schematic.

Chapter 3 Approach

3.1 Measurement Limitations

Optical imaging measurements have limitations to their temporal and spatial resolutions. These limitations are due to the uncertainty principle. The uncertainty principle is a well known property in quantum mechanics that limits the process of measurement. The uncertainty relation is given by $\Delta X \cdot \Delta P \geq \frac{\hbar}{2}$, meaning if anything is small in position space it will be large in transform or momentum space. This is a problem in a lot of optical system measurements. If the momentum resolution is increased there will be a loss of resolution in position and vice versa.[2] This also produces difficulties in trying to obtain spectroscopic information on a physical object when adjusting for good resolution in the time domain. Therefore by the uncertainty relation high resolution for position, momentum, frequency and time cannot be measured simultaneously. However, by using two local oscillator fields in an optical imaging system, high resolutions for the distributions of x, p, ω, and t can be obtained simultaneously surpassing the uncertainty principle.[15]

3.2 Previous Approach: Two-Window Technique

Previously a paper by K. F. Lee [2] showed that using two local oscillator fields in a balanced heterodyne detection scheme could be used to determine the Wigner distributions for optical fields. They called this the two-window technique [2,16]. The two-window technique uses two local oscillator beams, a small (focused) beam and a big (collimated) beam. This allowed independent control of position and momentum resolution. The small beam in the x-p representation in Figure 6 has a higher resolution in position. The big beam has a higher resolution in momentum. When these two oscillator beams are phase locked at 5 kHz, the shaded area in Figure 6 is the phase lock position and momentum resolution. By using simple algebra one can see that the x-p resolution of the two-window technique can easily suppress the uncertainty principle. The ratio of the sigma for the small beam and the big beam is one over ten in this experiment.
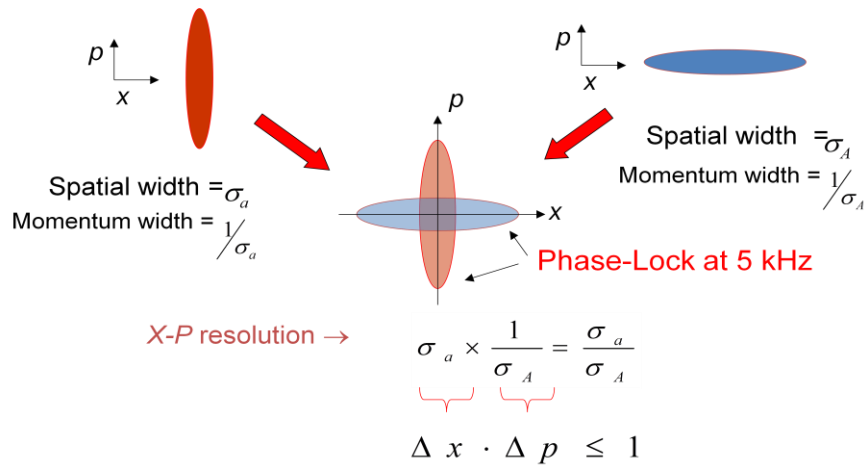
Figure 6 shows two local oscillator beams used to achieve independent control of position and momentum resolution of the measurement.

The Wigner distribution [17,18] is related to a Fourier Transform pair of position and momentum coordinates. This is called optical phase-space tomography [2,19]. It was previously predicted that a four-window technique could be developed by combining the two-window technique with the Wigner distribution for ω and t. By using low-coherence light the four-window technique can be used for biomedical imaging[2]. Low coherence tomography with two variables such as ω and p has been used previously to obtain information about changes in cell nuclei. Changes in cell nuclei can indicate cancer or inflammatory diseases [8,9,10].

3.3 Current Approach: Four-Window Technique

For this project two local oscillator (LO) fields were used to develop a four-window heterodyne detection system to measure the OPSTFT [15]. Figures 7a and 7b show the two local oscillator fields. "A local oscillator (LO) field is a phase coherent superposition of two fields i.e. a focused and a collimated Gaussian field."[15] For x-p pair, the focused LO has a spatial width $\Delta x_a = a$. The collimated LO has a spatial width of $\Delta x_A = A$. For ω-t pair, the focused LO has a wide optical spectrum with a bandwidth of $\Delta \omega_a = \alpha$.

6

Whereas the collimated LO has a narrow optical spectrum with a bandwidth of $\Delta\omega_A = \beta$. To be able to measure x and p simultaneously the focused LO Gaussian beam supplies the position resolution. At the same time, the collimated LO Gaussian beam supplies the momentum resolution. Therefore the product $\Delta x_a \cdot \Delta p_A = a \cdot \frac{1}{A} \leq 1$ overcomes the uncertainty principle limit. This product is represented in Figure 7a as the overlapping shaded area. The same idea applies; where the narrowband LO beam supplies the spectra resolution. The broadband LO beam provides the path-length resolution. The product $\Delta\omega_A \cdot \Delta t_a = \beta \cdot \frac{1}{\alpha} \leq 1$ also overcomes the uncertainty limit. This is represented in Figure 7b as the overlapping shaded area.

(a)

(b)
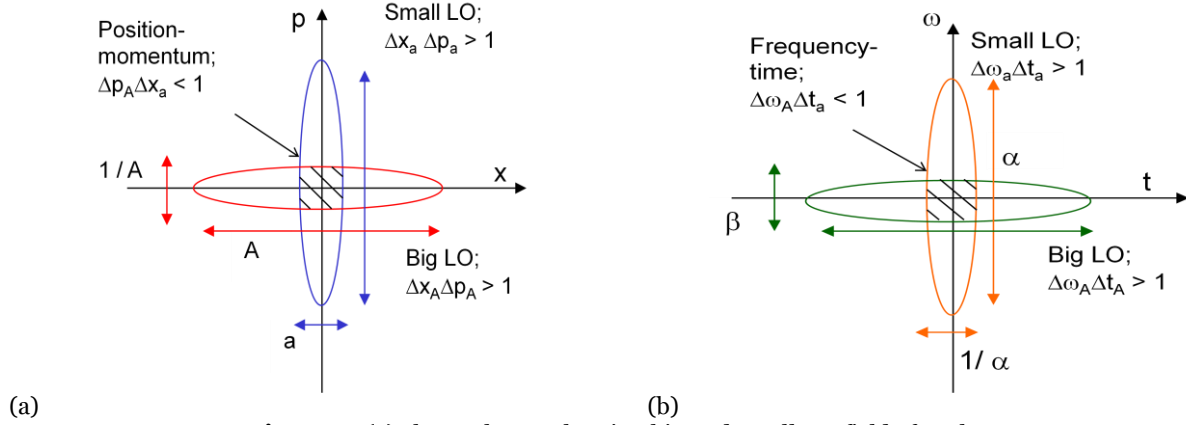
Figure 7 (a) shows the overlapping big and small LO fields for phase-space while (b) shows the overlapping big and small LO fields for frequency-time.

The four-window heterodyne detection system, including the two local oscillators, is shown in a schematic setup in Figure 8. In the schematic setup, scanning mirror M1 gives the transverse position $(d_x = x_\perp)$. Scanning lens L2 gives the transverse momentum $(d_p = p_\perp)$. Changing the tunable filter gives d_ω and the path delay of the signal beam gives τ. This provides the OPSTFT measurement. The fields for the LO and signal beams are in the plane of the detector, Z_D. The fields, in terms of the input field Z=0, are given in Equations (5) and (6), respectively.[15]

$$E_{LO}(x' - d_x, \omega - d_\omega, z_D) = \sqrt{\frac{k}{i2\pi f}} \int e^{i\frac{k(x-x')^2}{2f}} e^{-i\frac{kx^2}{2f}} E_{LO}(x - d_x, \omega - d_\omega, z = 0)\, dx \qquad (5)$$

$$E_S(x', \omega, z_D) = \sqrt{\frac{k}{i2\pi f}} \int e^{i\frac{k(x-x')^2}{2f}} e^{-i\frac{kx^2}{2f}} E_S(x, \omega, z = 0)\, dx \qquad (6)$$

The balanced heterodyne detection subtracts the photocurrents from the photodiodes at D_1 and D_2. The spectrum analyzer (S/A) measures the beat amplitude V_B. The overlapping of the two LO fields and the signal (S) field is represented by V_B. The beat amplitude is in the plane of the detector where Z= Z_D.[15]

$$V_B(d_x, d_\omega) = \int dx' \int d\omega \, E_{LO}^*(x' - d_x, \omega - d_\omega, z_D) E_S(x', \omega, z_D) \tag{7}$$

The output from the spectrum analyzer is then squared by the low noise multiplier (X²). The multiplier output is the beat amplitude squared $|V_B|^2$.[15]

$$|V_B(d_x, d_\omega)|^2 = \int d\omega \int dx E_{LO}^*(x - d_x, \omega - d_\omega) E_S(x', \omega) \, e^{-ikd_p x/f} e^{-i\omega\tau}$$
$$\times \int d\omega' \int dx' E_{LO}(x' - d_x, \omega' - d_\omega) E_S^*(x', \omega') \, e^{-ikd_p x'/f} e^{-i\omega'\tau} \tag{8}$$

A variable transformation is then made where $x = x_o + \frac{\eta}{2}, \omega = \omega_o + \frac{\eta_\omega}{2}, x' = x_o - \frac{\eta}{2}, \omega' = \omega_o - \frac{\eta_\omega}{2}$.[15] A simple substitution can be made since the Jacobian transform is 1. The squared beat signal is then written as

$$|V_B|^2 = \int d\omega_o dn_\omega dx_o d\,\eta E_{LO}^* \left(x_o - d_x + \frac{\eta}{2}, \omega_o - d_\omega + \frac{\eta_\omega}{2} \right) E_{LO} \left(x_o - d_x - \frac{\eta}{2}, \omega_o \right.$$
$$\left. - d_\omega - \frac{\eta_\omega}{2} \right) \tag{9}$$
$$\times E_S^* \left(x_o - \frac{\eta}{2}, \omega_o - \frac{\eta_\omega}{2} \right) E_S \left(x_o + \frac{\eta}{2}, \omega_o + \frac{\eta_\omega}{2} \right) e^{-i\frac{kd_p\eta}{f}} e^{-i\eta_\omega\tau}$$

The general definition of the Wigner distribution is the Fourier transform of the two point coherence function.

$$W(x, p) = \int \frac{d\epsilon}{2\pi} \exp(i\epsilon p) \langle \varepsilon^* \left(x + \frac{\epsilon}{2} \right) \varepsilon(x - \frac{\epsilon}{2}) \rangle \tag{10}$$

The inverse transform of W(x, p) for the light field is

$$\varepsilon^* \left(x + \frac{\epsilon}{2} \right) \varepsilon \left(x - \frac{\epsilon}{2} \right) = \int \exp(-i\epsilon p) \, W(x, p) dp. \tag{11}$$

This definition is used to rewrite the signal field.[15]

$$E_S^* \left(x_o + \frac{\eta}{2}, \omega_o + \frac{\eta_\omega}{2} \right) E_S \left(x_o - \frac{\eta}{2}, \omega_o - \frac{\eta_\omega}{2} \right) = \int e^{-i\eta p} e^{-i\eta_\omega t} W_S(x_o, p, \omega_o, t) dp dt \tag{12}$$

The square beat signal is rewritten by substituting Eq. (12) into Eq. (9).[15]

$$|V_B|^2 = \int d\omega_o d\eta_\omega dx_o d\eta E_{LO}^* \left(x_o - d_x + \frac{\eta}{2}, \omega_o - d_\omega + \frac{\eta_\omega}{2} \right)$$

$$\times E_{LO} \left(x_o - d_x - \frac{\eta}{2}, \omega_o - d_\omega - \frac{\eta_\omega}{2} \right) \qquad \text{(13)}$$

$$\times W_S(x_o, p, \omega_o, t) e^{-i\eta\left(\frac{kd_p}{f}+p\right)} e^{-i\eta_\omega(\tau+t)}$$

By using the Wigner distribution definition the Wigner function of the LO field can be written[15]

$$W_{LO}\left(x_o - d_x, p + \frac{kd_p}{f}, \omega_o - d_\omega, t - \tau\right) = \int d\eta d\eta_\omega \, e^{i\eta\left(\frac{kd_p}{f}+p\right)} e^{i\eta_\omega(t-\tau)} \times$$

$$E_{LO}^*\left(x_o - d_x, p + \frac{kd_p}{f}, \omega_o - d_\omega + \frac{\eta}{2}\right) \times E_{LO}\left(x_o - d_x - \frac{\eta}{2}, \omega_o - d_\omega - \frac{\eta_\omega}{2}\right). \qquad \text{(14)}$$

The square beat signal can then be written in terms of W_{LO} and W_S where the notation is changed to $x_o \to x$ and $\omega_o \to \omega$.[15]

$$|V_B|^2 = \int dx \int d\omega \int dp \int dt \, W_{LO}\left(x_o - d_x, p + \frac{kd_p}{f}, \omega_o - d_\omega, t - \tau\right) W_S(x, p, \omega, t) \qquad \text{(15)}$$

From Eq. (15) it is seen that $|V_B|^2$ is directly proportional to the convolution integral of the Wigner distributions. W_{LO} is in the plane of lens L1 and W_S is in the plane of lens L2. For the experiment the LO fields are engineered in the form of E_{LO} for a broadband light source.[15]

$$E_{LO}(x, \omega) = E_o \left[\exp\left(-\frac{x^2}{2a^2}\right) \exp\left(-\frac{\omega^2}{2\alpha^2}\right) + \gamma \exp\left(-\frac{x^2}{2A^2}\right) \exp\left(-\frac{\omega^2}{2\beta^2}\right) e^{i\emptyset} \right] \qquad \text{(16)}$$

The relative amplitude and phase are represented by γ and $\emptyset$. For the LO fields to be a Gaussian function a single mode fiber with a tunable bandpass Gaussian filter can be used. The LO Wigner function can then be written in terms of the phase dependent part.[15]

$$W_{LO}(x, p, \omega, t)$$

$$\propto exp\left[\frac{2x^2}{A^2} - 2a^2 p^2 + \frac{2\omega^2}{\alpha^2} - 2\beta^2 t^2\right] \cos(2xp + 2\omega t + \emptyset) \qquad \text{(17)}$$

$$\cong \cos(2xp + 2\omega t + \emptyset)$$

The approximation that $A \gg a$ and $\alpha \gg \beta$ allows the signal field to limit the integration in Eq. (12). The focused and collimated LO fields are phase-locked at $\emptyset$Hz. With the use of the heterodyne detection scheme the beat signal of the focused LO field is Ω_ωMHz. The beat signal of the collimated LO field is $\Omega_\omega MHz + \emptyset KHz$. The spectrum analyzer has a bandwidth of $100KHz > \emptyset KHz$ which is centered at Ω_ωMHz. The spectrum analyzer

measures V_B. The output of the spectrum analyzer is sent to the multiplier which gives $|V_B|^2$. The output of the multiplier is sent to the lock-in amplifier. By substituting Eq. (14) into Eq. (12), $|V_B|^2$ is directly proportional to the real (S_R) and imaginary parts (S_I). Notation is changed for simplicity $d_x \to x_o, \frac{kd_p}{f} \to p_o, d_\omega \to \omega_o, \tau \to t_o$. S_R corresponds to the in-phase amplitude and S_I corresponds to the out-of phase amplitude.[15]

$$
\begin{aligned}
|V_B|^2 \propto K(x_o, p_o, \omega_o, t_o) &\propto S_R + iS_I \\
&\propto \int dx' dp' d\omega' dt' e^{[2i(x'-x_o)(p'-p_o)+2i(\omega'-\omega_o)(t'-t_o)]} W_S(x', p', \omega', t') \\
&\propto \langle E_S^*(x_o, \omega_o) E_S(p_o, t_o) \rangle \exp(ix_o p_o + i\omega_o t_o)
\end{aligned}
\tag{18}
$$

From Eq. (18) it is seen that $|V_B|^2$ is directly proportional to the Kirkwood-Rihaczek distribution $K(x_o, p_o, \omega_o t_o)$. By linear transformation Eq. (18) is then inverted to give the Wigner phase-space and time-frequency function (OPSTFT).[15]

$$
\begin{aligned}
W_S \propto &\int dx_o dp_o d\omega_o dt_o \cos[2(x - x_o)(p - p_o) \\
&+ 2(\omega - \omega_o)(t - t_o)] S_R(x_o, p_o, \omega_o, t_o) \\
+ &\int dx_o dp_o d\omega_o dt_o \sin[2(x - x_o)(p - p_o) + 2(\omega - \omega_o)(t - t_o)] S_I(x_o, p_o, \omega_o, t_o)
\end{aligned}
\tag{19}
$$

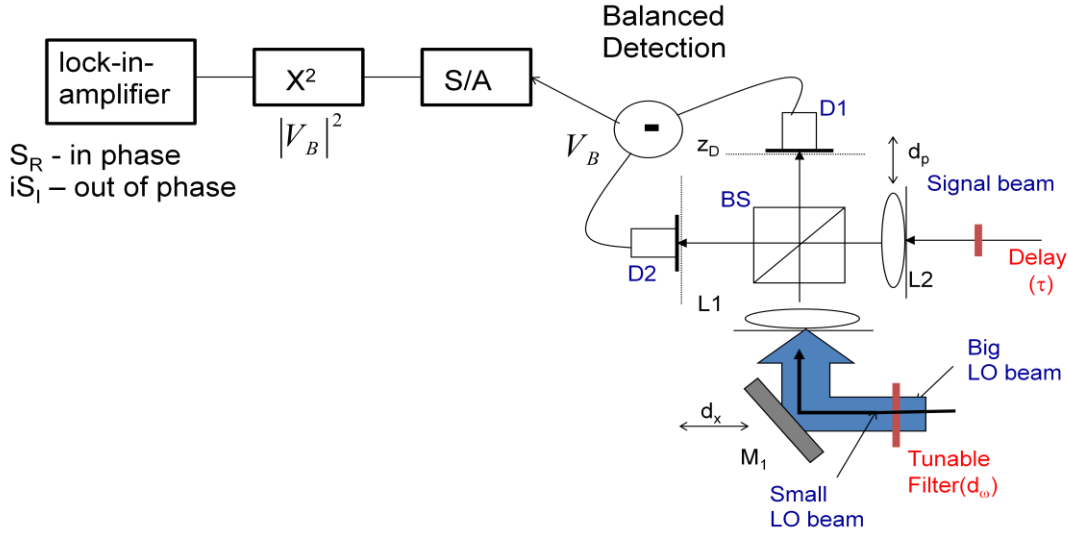This is the OPSTFT measurement of the signal field.

Figure 8 shows the schematic for the four-window technique to measure the OPSTFT. The experimental setup uses balanced heterodyne detection and two LO fields.

Chapter 4 Simulation

4.1 Bone-Tissue Interface (A Wire Function Simulation)

A simulation was performed to simulate the detection of disease by using optical phase-space-time-frequency tomography. The first simulation is for the bone-tissue interface of a rat tail. Diseases such as lymphedema, that cause tissue swelling, will cause the gap between the bone and tissue to be smaller. Figure 9 shows the bone-tissue interface.
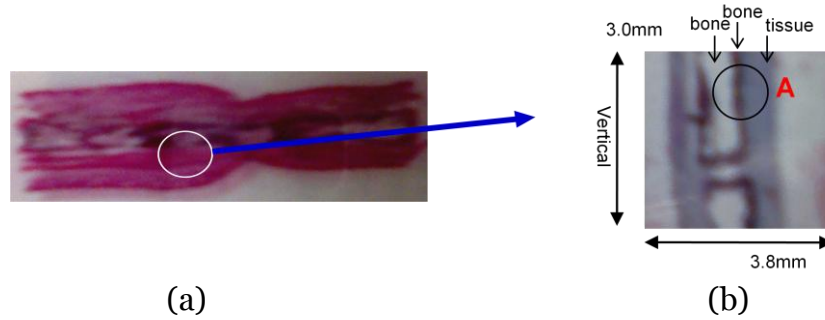

| (a) | (b) |

Figure 9 (a) shows the cut rat tail with the circle indicating the swollen tissue-bone interface and (b) shows a cross section of the rat tail on a slide where the circle indicates the bone-tissue interface.

The OPSTFT simulation can provide six distributions, $x - p$, $\omega - t$, $\omega - x$, $t - x$, $\omega - p$, and $t - p$. These provide new valuable information about the scattered light field through the bone-tissue interface. The simulation was written using Mathematica. Independent variables, a, 1/A, 1/α, and β were chosen to be small. The thin wire diameter was chosen to be 0.6mm. A slit function was used in Mathematica to represent the wire (slitfun[x]=If[-0.3mm≤ x ≥0.3mm, 0.0,1.0]). To obtain the light field scattered after the wire, $\varepsilon_{wire}(x,t)$, the slit function was multiplied by the wave field of a Gaussian beam as seen in Eq. (20).

$$\varepsilon_{wire}(x,t) \propto \exp\left[-\frac{x^2}{2\sigma_x^2}\right]\exp\left[i\frac{kx^2}{2R}\right]\exp\left[-\frac{t^2}{2\sigma_t^2}\right]\exp\left[i\omega_c t\right] \times slitfun[x] \qquad \textbf{(20)}$$

In Eq. (20) σ_x is the spatial bandwidth, σ_t is the temporal bandwidth, R is the radius of curvature, and ω_c is the center or carrier frequency. This field has been previously used to explore the phase-space interface. However, the addition of time-frequency distributions being included with phase-space distributions in the Wigner distribution has not been explored before.[2,15] For the simulation the following values were used σ_x = 0.85mm, σ_t = 200fs, R = -10000mm and ω_c = 0. The numerical Fourier transform of $\varepsilon_{wire}(x,t)$ was done by generating 20 position coordinate points and 20 time coordinate

points from $\varepsilon_{wire}(x,t)$. The Fourier transform of $\varepsilon_{wire}(x,t)$ gives $\varepsilon_{wire}(p,\omega)$. Using these two fields the Kirkwood-Richaczek distribution was generated, see Eq. (21).

$$K(x,p,\omega,t) = \varepsilon_{wire}^*(x,t)\varepsilon_{wire}(p,\omega)\exp\,(ixp - i\omega t) \tag{21}$$

To explore the phase-space distribution, ω and t were set to zero. Plots were generated for the real and imaginary parts of $K(x,p,0,0)$ as presented in Figure 10a and 10b, respectively. The units are millimeters for position, radian per millimeter for momentum, 10^{13}Hz for frequency and 10^{-13}s for time. The frequency plotted is the difference from the center frequency (ω - ω_c). Time is plotted as the difference from the zero time delay (t - τ) where τ=0. When x and p are set to zero then $K(0,0,\omega,t)$ is zero. This is because at the point (x=0, p=0) the beat signal $|V_B^2|$ is zero. To explore a nontrivial result a nonzero point was chosen (x=0.4, p=0). The real and imaginary parts of $K(0.4,0,\omega,t)$ are plotted in Figures 10c and 10d, respectively.
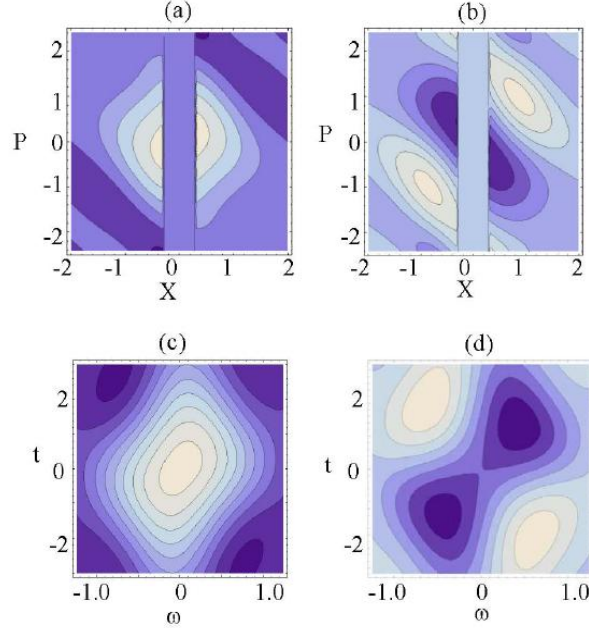
Figure 10 The KR distribution for the wave field after the wire as in Eq. (20) and Eq. (21). (a) shows the real part of K(x,p,00) and (b) shows the imaginary part of K(x,p,00). (c) and (d) show the real and imaginary parts of K(0.4,0,ω,t) respectively.

The Wigner distribution was calculated using Mathematica to perform the numerical integration required to linear transform $K(x,p,\omega,t)$.

$$W_s(x,p,\omega,t) \propto \int e^{[2i(x-x_o)(p-p_o)+2i(\omega-\omega_o)(t-t_o)]}K(x_o,p_o,\omega_o,t_o)dx_o dp_o d\omega_o dt_o \tag{22}$$

12

Mathematica plots were generated for the six OPSTFT distributions. The plot of $W(x, p, 0,0)$ in Figure 11a is interesting because it shows a phase-space oscillation along the x=0 axis. This oscillation is due to two spatially separated wave packets interfering with one another after the wire. This plot demonstrates the fact that the Wigner function can have negative values. [12,13,14] The oscillations show evidence of sub-Planck phase-space structure. [21,22] The plot of $W(0,0, \omega, t)$ in Figure 11b shows that even though $K(0,0, \omega, t)$ is zero everywhere, the Wigner distribution for the point (x=0, p=0) is not. The cause for this difference is that the Kirkwood-Richaczek distribution is more appropriate for describing the local properties of a wave function. The Wigner function is more appropriate for describing wave properties of a particle wave function.[15,17] To again demonstrate that the Wigner function can be negative, a plot of $W(0,2, \omega, t)$ in Figure 11c, is given. Figure 11c is the inverse of Figure 11b because $W(0,2,0,0)$ has a negative value. Oscillation and interference behavior is again observed, this time along the momentum coordinate. Plots of $W(0, p, 0, t)$ and $W(0, p, \omega, 0)$ show oscillations. This illustrates that the interference of two spatially separated wave packets in phase-space does affect the momentum distribution within time and frequency domains. Plots of $W(x, 0,0, t)$ and $W(x, 0, \omega, 0)$are also provided in Figures 11f and 11g.
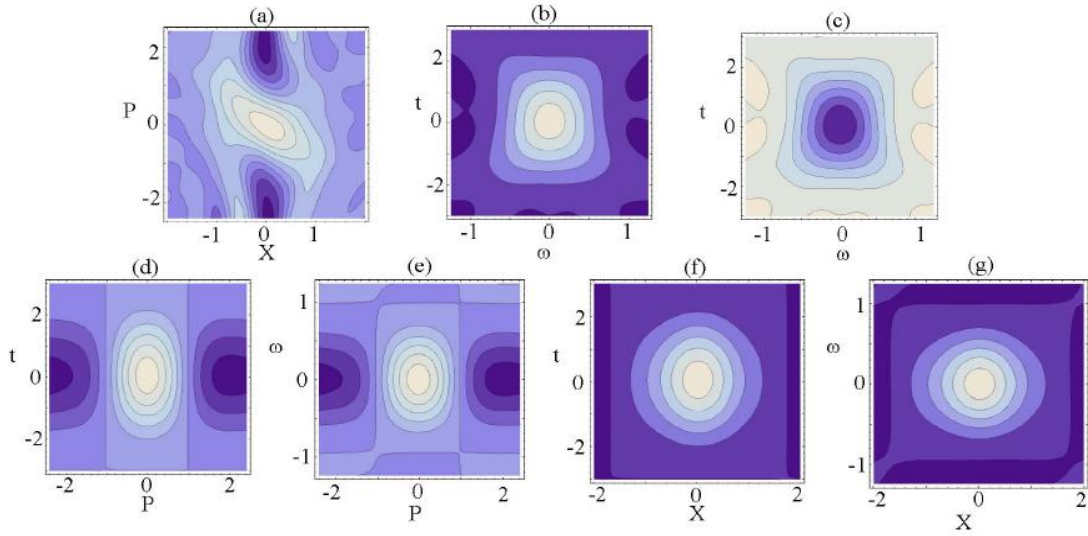
Figure 11 The OPSTFT for the wave field after the wire as in Eq. (20).
(a) $W(x, p, 0,0)$, (b) $W(0,0, \omega, t)$, (c) $W(0,2, \omega, t)$, (d) $W(0, p, 0, t)$,
(e)$W(0, p, \omega, 0)$, (f) $W(x, 0,0, t)$, and (g) $W(x, 0, \omega, 0)$.

4.2 Spectra Response of Tissue (An Absorption Filter Simulation)
The second simulation was performed to simulate the spectra response of diseased tissue by using optical phase-space-time-frequency tomography. Diseases such as

lymphedema cause tissue swelling. The density of the tissue changes as the tissue swells. In cancer cells the density of the cell nucleus changes as the cells become more neoplastic. The change in tissue density changes the spectra response of tissue. Figure 12 shows swollen tissue and the representation of the tissue as an absorption filter.
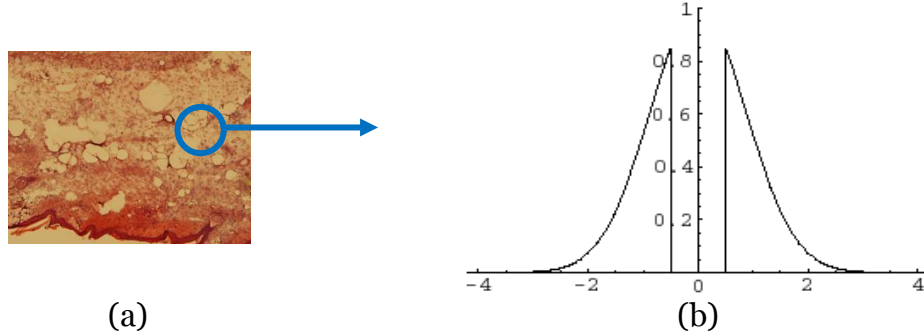

<center>(a)   (b)</center>

Figure 12 (a) shows swollen tissue with the circle indicating the portion to be investigated (b) shows the representation of the tissue as an absorption filter as in Eq. (23).

The OPSTFT simulation can provide six distributions, $x - p$, $\omega - t$, $\omega - x$, $t - x$, $\omega - p$, and $t - p$. These provide new information about the light field after passing through tissue. The absorption filter, with a bandwidth of 2THz, is represented in Mathematica as (slitfun[x]=If[-0.1≤ x ≤0.1, 0.0, 1.0]). To make the simulation of the OPSTFT measurement easier the calculations begin in the spectra domain. Allowing the field to be represented as a Gaussian beam multiplied by the absorption filter function.[15]

$$\varepsilon_{filter}(x,\omega) \propto \exp\left[-\frac{x^2}{2\sigma_x^2}\right]\exp\left[i\frac{kx^2}{2R}\right]\exp\left[-\frac{(\omega-\omega_c)^2}{2\sigma_\omega^2}\right] \times slitfun[x] \tag{23}$$

In Eq. (23) σ_ω is the spectra bandwidth and the following values were used for the simulation; σ_x = 0.85 mm, σ_t = 5.0 THz, R = -10000 mm and ω_c = 0. Using Mathematica, $\varepsilon_{filter}(x,\omega)$ was Fourier transformed to $\varepsilon_{filter}(p,t)$. These two field equations were then used to generate the Kirkwood-Richaczek distribution.[15]

$$K(x,p,\omega,t) = \varepsilon_{filter}^*(x,\omega)\varepsilon_{filter}(p,t)\exp(ixp + i\omega t) \tag{24}$$

Mathematica plots of the KR distribution were then generated by choosing values for two of the variables. In Figure 13a and 13b the absorption band can clearly be seen for the real and imaginary parts of $K(0,0,\omega,t)$. When ω=0 and t=0 the beat signal is zero as

<center>14</center>

well as the KR distribution. In order to explore the nontrivial solution, values were chosen to be ω=0.2 and t=0. Plots of the real and imaginary parts of $K(x, p, 0.2, 0)$ are shown in Figure 13c and 13d.
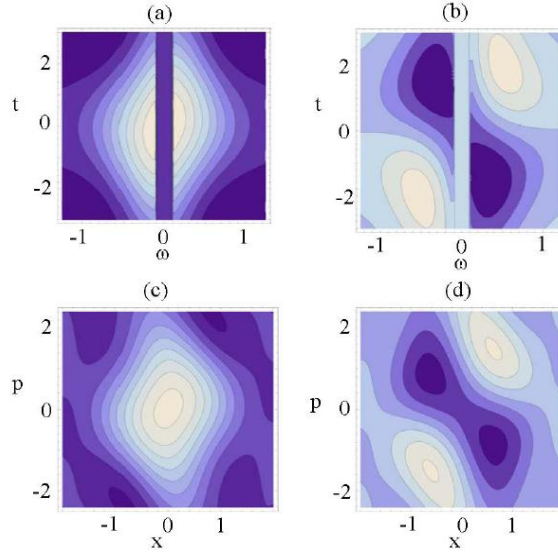

Figure 13 The KR distribution for the wave field after the wire as in Eq. (23) and Eq. (24). (a) shows the real part of K(0,0,ω,t) and (b) shows the imaginary part of K(0,0,ω,t). (c) and (d) show the real and imaginary parts of K(x,p,0.2,0) respectively.

Again the Wigner distribution was calculated by using Mathematica to perform the numerical integration required to linear transform $K(x, p, \omega, t)$ as in Eq. (18). When x is set to zero and p is set to zero, a time-frequency oscillation can be seen along the $\omega = 0$ axis in Figure 14a. The time-frequency interference in the plot of $W(0,0,\omega,t)$ is due to two spectrally separated wave packets interfering after the filter. This interference was observed previously.[22] To investigate phase-space, values were set to be ω=0 and t=0, Figure 14b shows $W(x, p, 0, 0)$. Again the Wigner function has a negative value, the plot of $W(x, p, 0, 3)$ in Figure 14c is the inverse of Figure 14b. This is because $W(0,0,0,3)$ has a negative value. Oscillation and interference behavior is again observed, this time along the time coordinate. The oscillation can be seen in the plots of $W(0, p, 0, t)$ and $W(x, 0, 0, t)$, shown in Figures 14d and 14f, correspondingly. This illustrates that the interference of two spatially separated wave packets in frequency-time does affect the time distribution within position and momentum domains. Plots of $W(0, p, \omega, 0)$ and $W(x, 0, \omega, 0)$ are also provided in Figures 14e and 14g.[15]
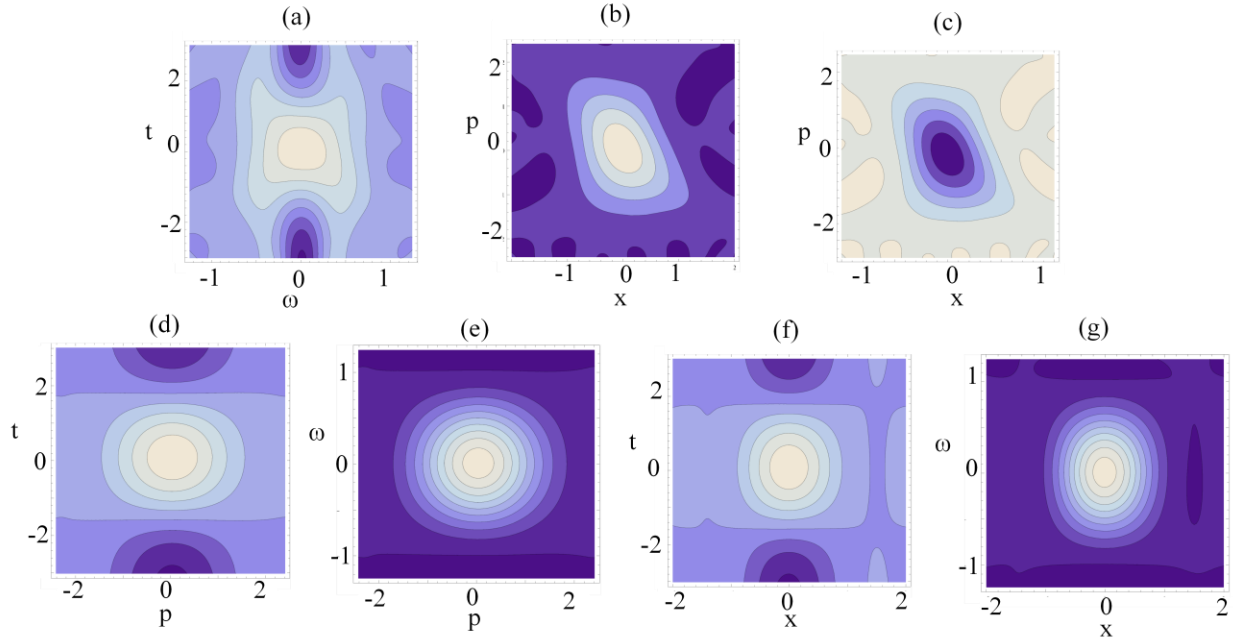
Figure 14 The OPSTFT for the wave field after the wire as in Eq. (22).
(a) $W(0,0,\omega,t)$, (b) $W(x,p,0,0)$, (c) $W(x,p,0,3)$, (d) $W(0,p,0,t)$,
(e) $W(0,p,\omega,0)$, (f) $W(x,0,0,t)$, and (g) $W(x,0,\omega,0)$.

Chapter 5 Conclusion

In Conclusion, by using balanced heterodyne detection, a four-window technique for measuring optical phase-space-time-frequency tomography has been developed. The four-window technique used two local-oscillators which allowed for independent control and simultaneous high resolution for position, momentum, frequency and time. This four-window technique can be applied to imaging tissue samples for the purpose of disease detection.

Works Cited

1.   Raymond W. Ruddon, *Cancer Biology,* 4th ed. (Oxford University Press, 2007).

2.   K. F. Lee, F. Reil, S. Bali, A. Wax, and J. E. Thomas, "Heterodyne measurement of Wigner distributions for classical optical fields." Opt. Lett. **24**, 1370-1372 (1999).

3.   R. N. Wax, "Nuclear morphology measurements using Fourier domain low coherence interferometry." Optics Express **13**, 4693-4697 (2005).

4.   Alberts, e. a., *Molecular Biology of The Cell,* 4th ed. (Garland Science, 2002).

5.   Robert A. Weinberg, *The Biology of Cancer,* 1st ed. (Garland Science, 2007).

6.   S. John, G. Pang, and Y. Yang, "Optical Coherence Propogation and Imaging in a Multiple Scattering Medium," J. Biomed. Opt. **1**, 180-191 (1996).

7.   A. F. Fercher, e. a., "Optical coherence tomography-principles and applications." Institute of Physics Publishing, **66**, 239-303 (2003).

8.   John W. Phytila, e. a., "In situ detection of nuclear atypia in Barrett's esophagus by using angle-resolved low-coherence interferometry." Gastrointestinal Endoscopy Journal **65**, 487-491 (2007).

9.   Adam Wax, e. a., "Prospective grading of neoplastic change in rat esophagus epithelium using angle-resolved low-coherence interferometry." J. Biomed. Opt. **10**, 0516041-05160410 (2005).

10.   John W. Pyhtila, e. a., "Fourier-domain angle-resolved low coherence interferometry through an edoscopic fiber bundle for light-scattering spectroscopy." Opt. Lett. **31**, 772-774 (2006).

11.   Genetic Science Learning Center, "Cell Size and Scale," *Learn.Genetics*, 24 January 2011, <http://learn.genetics.utah.edu/content/begin/cells/scale/> (21 November 2011)

12.   Ch. Kurtsiefer, T. Pfau, and J. Mlynek, "Measurement of the Wigner function of an ensemble of Helium atoms," Nature **386**, 150–153 (1997).

13.   D. Leibfried, T. Pfau, and C. Monroe, "Shadows and mirrors: reconstructing quantum states of atom motion," Phys. Today **51**(4), 22–28 (April 1998).

14.   K. Wodkiewicz and G. H. Herling, "Classical and non-classical interference," Phys. Rev. A **57**, 815–821 (1998).

15.   P. Rojas, R. Blaser, Y. M. Sua, and K. F. Lee, "Optical Phase-Space-Time-Frequency Tomography," Optics Express **19**(8), 7480-7490 (April 2011).

16. V. Bollen, Y. M. Sua, and K. F. Lee, "Direct measurement of the Kirkwood-Rihaczek distribution for the spatial properties of a coherent light beam," Phys. Rev. A **81**, 063826 (2010).

17. E. P. Wigner, "On the quantum correction for thermodynamic equilibrium," Phys. Rev. **40**, 749–759 (1932).

18. M. Hillery, R. F. O'Connell, M. O. Scully, and E. P. Wigner, "Distribution functions in physics: fundamentals," Phys. Rep. **106**, 121–167 (1984).

19. F. Reil and J. E. Thomas, "Observation of phase conjugation of light arising from enhanced backscattering in a random medium," Phys. Rev. Lett. **95**, 143903 (2005).

20. W. H. Zurek, "Sub-Planck structure in phase space and its relevance for quantum decoherence," Nature **412,** 712–717 (2001).

21. F. Toscano, D. A. R. Dalvit, L. Davidovich, and W. H. Zurek, "Sub-Planck phase-space structures and Heisenberg-limited measurements," Phys. Rev. A **73,** 023803 (2006).

22. S. John, G. Pang, and Y. Yang, "Optical Coherence Propagation and Imaging in a Multiple Scattering Medium," J. Biomed. Opt. **1**, 180–191 (1996).